ELSEVIER

Comput. Methods Appl. Mech. Engrg. 190 (2001) 3623–3644

Computer methods in applied mechanics and engineering

www.elsevier.com/locate/cma

Local entropy generation in an impinging jet: minimum entropy concept evaluating various turbulence models

S.Z. Shuja, B.S. Yilbas *, M.O. Budair

Department of Mechanical Engineering, King Fahd University of Petroleum and Minerals, P.O. Box 1913, Dhahran 31261, Saudi Arabia

Received 16 November 1999; received in revised form 8 March 2000

Abstract

Second law analysis techniques have been widely used to evaluate the sources of irreversibility in fluid flow systems. The same technique may be used to evaluate the various turbulence models. In the present study, a local entropy generation rate is computed for a fluid jet impinging on a heated wall. The standard k–ε, low-Reynolds number k–ε and two Reynolds stress models are introduced to account for the turbulence. A numerical scheme employing a control volume approach is used to solve the governing equations. The predictions are, then, compared with the experimental findings in the literature. The local volumetric entropy generation in the region close to the stagnation point is used to evaluate the turbulence models. The entropy generation gives information about the magnitude of viscous dissipation in the flow field. The minimum energy concept alone may not be used to evaluate the various turbulence models, in which case, the experimental measurements are accompanied with the results of entropy analysis.

1. Introduction

An axisymmetric jet flow impinging vertically on a flat plate is used in many industrial applications: the cooling of electronic devices, the turbine blades, drying of industrial goods, laser processing of metals etc. The use of impinging jet enables to enhance heat and mass transfer rates in the stagnation region of an impingement surface. On the other hand, the turbulence models are, in general, tested for flows parallel to solid surface, therefore, they may be unable to present impinging flow extensively. Consequently, the jet impinging becomes important when testing the applicability of the existing turbulence models. Impinging jet studies for turbulence have indicated several problems in the existing turbulence models [1–3]. One of the problems encountered included that the standard k–ε model tended to overestimate the turbulent kinetic energy in the stagnation region. Moreover, the wall-reflection term in the stress equation model initiated by Gibson and Harper [4] has an adverse effect on the turbulence restriction mechanism near the impingement surface. Turbulent flow and heat transfer measurement on a curved surface with a fully developed round impinging jet was carried out by Lee et al. [5]. They used an image processing system to monitor the fluid action close to the stagnation region. Nishino et al. [6] investigated the turbulence in the region of an axisymmetric impinging jet flow. The state of turbulence was studied by means of an invariant map of the turbulence stress anisotropy. They indicated that the turbulence was close to an axisymmetric state in the

* Corresponding author. Tel.: +1-966-3-860-2540; fax: +1-966-3-860-2949.
E-mail address: bsyilbas@kfupm.edu.sa (B.S. Yilbas).

0045-7825/01/$ - see front matter
PII: S0045-7825(00)00291-7

Nomenclature

C_1, C_2, C_μ	coefficients in the turbulence models
D	jet inlet diameter
E	mean component of the rate of deformation of a fluid element
e	internal energy
f_1, f_2, f_μ	coefficient in the low-Reynolds number, k–ε model
H	mean enthalpy
h	r.m.s. fluctuating enthalpy
K	thermal conductivity
k	turbulent kinetic energy
l	distance between wall and nozzle
P	rate of production of R_{ij}
p	pressure
$\dot{q}$	constant heat flux over a specified area
R	Reynolds stress
Re	Reynolds number
S'''_{gen}	Volumetric entropy generation
s	entropy
r	distance in the radial direction
r^*	non-dimensional distance in the radial direction (r/D)
$\overline{S_H}$	source term in the energy equation
T	temperature
$\overline{u}$	average inlet velocity
U	velocity in an arbitrary direction
v'	r.m.s. fluctuating velocity in the radial direction
V	velocity in the radial direction
w'	r.m.s. fluctuating velocity in the axial direction
W	velocity in the axial direction
x	arbitrary direction
z	distance in the axial direction normal to the wall
z^*	non-dimensional distance in the axial direction normal to the wall (z/D)
Greek	
δ_{ij}	Kronecker delta
ε	energy dissipation
η	permutation symbol
θ	dimensionless temperature
κ	von karman's constant
λ	a fraction of $\overline{u}$ typically 0.03
μ	dynamic viscosity
Π	transport of R_{ij} due to turbulent pressure excluding strain interaction
ν	kinematic viscosity
Λ	transport of R_{ij} by diffusion
ρ	density
σ	Prandtl number
τ_w	shear stress at the wall
Φ	viscous dissipation
ϕ	arbitrary variable
χ	wall roughness parameter
Ω	transport of R_{ij} due to rotation
ω	rotational vector

Subscripts

i, *j*	arbitrary direction
eff	effective
jet	corresponding to the jet
l	laminar
t	turbulent
w	wall

stagnation region. They found negative production taking place in the wall vicinity when comparing the budget equation for the turbulence kinetic energy; in which case, the negative production was compensated by the pressure diffusion.

On the other hand, an extensive amount of theoretical work on the jet impingement was carried out previously by [7–10]. The numerical errors associated with some of the early simulations cited prevent any reliable assessment of the turbulence model accuracy. The standard k–ε and Reynolds stress models were compared with experimental results of heat transfer distribution [11] and some velocity and turbulence results within the stagnation region. The numerical solution was considered satisfactory, but variations between model and experiment were still evident. In this case, the standard k–ε model was shown to overpredict the heat transfer coefficient due to jet impingement, which was associated with the overprediction of the turbulent kinetic energy near the stagnation point. Although much effort has been directed toward improving such shortcoming in existing turbulence models, the progress has been hindered somewhat by the lack of detailed experimental data, particularly in the stagnation region. The assessment of various models mostly base on the comparison of the numerical simulations with the experimental findings. This approach may be limited by the lack of detailed experimental data and the varied specification of the flow field boundaries. However, the various turbulence models for given boundary conditions may be assessed using the concept of minimum irreversibility involvement in the flow field. In this case, the turbulence model that results in minimum entropy generation may give results closer to that obtained from the experiment. Moreover, it was suggested that an important relationship existed between the empirical components of the pure fluid-mechanics integral treatment, and the entropy generation extrema unveiled by the thermodynamic analysis [12].

In a flow field, non-equilibrium conditions prevail due to the exchange of momentum, energy and mass within the fluid and at the solid boundaries. The non-equilibrium phenomenon results in a continuous generation of entropy in the flow field. In most of the fluid system, exchange of momentum, mass and energy between the working fluid and the boundaries cause an increase in entropy which results in the destruction of energy. The entropy generation studies have influenced the design methodology of energy conversion systems [13,14]. However, extensive review on entropy generation minimization was carried out by Bejan [15]. He indicated the importance of entropy generation minimization in engineering systems. The numerical predictions of local entropy generation in a laminar impinging jet was studied by Drost and White [16]. They indicated that the entropy generation was concentrated in the boundary layer and an optimum jet Reynolds number minimizing the entropy generation in the impinging jet exists. Moreover, the results showed that the calculation of local entropy generation could provide useful information about the turbulence model employed.

The present study is carried out to assess the various turbulence models using the minimum entropy generation concept as an extension of previous work [17]. The jet impingement onto a limited area uniform heat flux plate is considered with the appropriate boundary conditions. Four models are selected to account for the turbulence. These include standard k–ε, low-Reynolds number k–ε, Reynolds stress model (RSTM-1) in which the generalized gradient diffusion model is considered for the scalars and the second Reynolds stress model (RSTM-2) in which full flux transport of energy and scalars are taken into account. The local entropy generation in the near and far field is computed for all the turbulence models introduced.

2. Turbulence models and entropy generation

The governing flow and energy equations for the axisymmetric impinging jet may be written in the Cartesian tensor notation as

The continuity:

$$\frac{\partial}{\partial x_i}(\rho U_i) = 0. \tag{1}$$

The momentum:

$$\frac{\partial}{\partial x_i}(\rho U_i U_j) = -\frac{\partial p}{\partial x_j} + \frac{\partial}{\partial x_i}\left[\mu\left(\frac{\partial U_i}{\partial x_j} + \frac{\partial U_j}{\partial x_i}\right) - \rho R_{ij}\right]. \tag{2}$$

The energy equation:

$$\frac{\partial}{\partial x_i}(\rho U_i H) = \frac{\partial}{\partial x_i}\left[\frac{\mu}{\sigma}\frac{\partial H}{\partial x_i} - \rho R_{ih}\right] + \overline{S_H}. \tag{3}$$

Four models are considered to account for the turbulence. These include the standard k–ε, low-Reynolds number k–ε, Reynolds stress model in which the generalized gradient diffusion is considered for the scalars (RSTM-1) and Reynolds stress model in which full flux transport of energy and scalars are taken into account (RSTM-2).

2.1. The standard k–ε model

The k–ε model focuses on the mechanisms that affect the turbulent kinetic energy [18]. To compute the Reynolds stress with the k–ε model an extended Boussinesq relationship is used

$$-\rho R_{ij} = \mu_t\left(\frac{\partial U_i}{\partial x_j} + \frac{\partial U_j}{\partial x_i}\right) - \frac{2}{3}\rho k \delta_{ij}. \tag{4}$$

The effect of the viscous stresses on the mean flow kinetic energy (k) can be split into two parts: (i) the transport of k due to viscous stress and (ii) the viscous dissipation of mean kinetic energy. Turbulent transport of heat is modelled similarly.

$$-\rho R_{ih} = \frac{\mu_t}{\sigma_h}\frac{\partial h}{\partial x_i}, \tag{5}$$

with $\sigma_h = 1$.

The standard k–ε model uses the transport equations for k and ε, where ε is the turbulent kinetic energy dissipation. These equations are

$$\frac{\partial}{\partial x_i}(\rho U_i k) = \frac{\partial}{\partial x_i}\left[\left(\mu + \frac{\mu_t}{\sigma_k}\right)\frac{\partial k}{\partial x_i}\right] + 2\mu_t E_{ij}\cdot E_{ij} - \rho\varepsilon \tag{6}$$

and

$$\frac{\partial}{\partial x_i}(\rho U_i \varepsilon) = \frac{\partial}{\partial x_i}\left[\left(\mu + \frac{\mu_t}{\sigma_\varepsilon}\right)\frac{\partial \varepsilon}{\partial x_i}\right] + C_1\frac{\varepsilon}{k}2\mu_t E_{ij}\cdot E_{ij} - C_2\rho\frac{\varepsilon^2}{k}, \tag{7}$$

Table 1
The constants employed in the k–ε model

C_μ	C_1	C_2	σ_k	σ_ε
0.09	1.44	1.92	1.00	1.00

where μ_t is modelled as

$$\mu_t = \rho C_\mu \frac{k^2}{\varepsilon}. \tag{8}$$

The constants appearing in the above transport equations are given in Table 1.

2.2. Low-Reynolds number k–ε model

The standard k–ε model may not be applicable at low-Reynolds number; in this case, alterations in k–ε model become necessary. The wall damping is required ensuring the viscous stresses present in the viscous sub-layer adjacent to solid wall. This modified k–ε model allocating the low-Reynolds number is

$$\mu_t = \rho C_\mu f_\mu \frac{k^2}{\varepsilon}, \tag{9}$$

$$\frac{\partial}{\partial x_i}(\rho U_i k) = \frac{\partial}{\partial x_i}\left[\left(\mu + \frac{\mu_t}{\sigma_k}\right)\frac{\partial k}{\partial x_i}\right] + 2\mu_t E_{ij}\cdot E_{ij} - \rho\varepsilon, \tag{10}$$

$$\frac{\partial}{\partial x_i}(\rho U_i \varepsilon) = \frac{\partial}{\partial x_i}\left[\left(\mu + \frac{\mu_t}{\sigma_\varepsilon}\right)\frac{\partial \varepsilon}{\partial x_i}\right] + C_{1\varepsilon} f_1 \frac{\varepsilon}{k} 2\mu_t E_{ij}\cdot E_{ij} - C_{2\varepsilon} f_2 \rho \frac{\varepsilon^3}{k}. \tag{11}$$

C_μ, C_1 and C_2 are the constants appearing in the standard k–ε, and f_μ, f_1 and f_2 are the wall-damping functions. Lam–Bremhosts wall-damping functions may be used in this regard [18]

$$f_\mu = [1 - \exp(-0.0165 Re_z)]^2 \left(1 + \frac{20.5}{Re_t}\right), \tag{12}$$

$$f_1 = \left(1 + \frac{0.05}{f_\mu}\right)^3 \quad \text{and} \quad f_2 = 1 - \exp\left(-Re_t^2\right), \tag{13}$$

where

$$Re_z = \frac{k^{1/2} z}{\nu}. \tag{14}$$

2.3. Reynolds stress equation model

2.3.1. Reynolds stresses (R_{ij})

The Reynolds stress model is based on the second-moment closure [19,20]. The transport equation of the Reynolds stress (R_{ij}) is

$$\frac{\partial}{\partial x_m}(U_m R_{ij}) = P_{ij} + \Lambda_{ij} - \varepsilon_{ij} + \Pi_{ij} + \Pi^w_{ij}, \tag{15}$$

where $P, \Lambda, \varepsilon, \Pi$ and Π^w are the rate of production, transport by diffusion, rate of dissipation, transport due to turbulent pressure excluding strain interactions and transport due to wall reflection, respectively. Eq. (15) consists of six partial differential equations: one for the transport of each of the six independent Reynolds

stresses. The production term (P_{ij}), diffusion (Λ_{ij}), dissipation (ε_{ij}), transport due to turbulent pressure (Π_{ij}) and the wall reflection (Π_{ij}^{w}) terms may be written as

Production term:

$$P_{ij} = -\left(R_{im}\frac{\partial U_j}{\partial x_m} + R_{jm}\frac{\partial U_i}{\partial x_m} \right). \tag{16}$$

Diffusion term:

$$\Lambda_{ij} = \frac{\partial}{\partial x_m}\left(\frac{v_t}{\sigma_k}\frac{\partial R_{ij}}{\partial x_m} \right) \tag{17}$$

with

$$v_t = C_\mu \frac{k^2}{\varepsilon};\ C_\mu = 0.09 \quad \text{and} \quad \sigma_k = 1.0. \tag{18}$$

Dissipation rate:

$$\varepsilon_{ij} = \frac{2}{3}\varepsilon\delta_{ij}, \tag{19}$$

where ε is the dissipation rate of turbulent kinetic energy defined earlier and δ_{ij} is the Kronecker delta.

Transport due to turbulent pressure:

$$\Pi_{ij} = \Pi_{ij1} + \Pi_{ij2} = -C_1\frac{\varepsilon}{k}\left(R_{ij} - \frac{2}{3}k\delta_{ij} \right) - C_2\left(P_{ij} - \frac{2}{3}p\delta_{ij} \right) \tag{20}$$

with

$$C_1 = 1.8 \quad \text{and} \quad C_2 = 0.6$$

The wall reflection term: [20]

$$\Pi_{ij}^{w} = \left[C_{1w}\frac{\varepsilon}{k}\begin{pmatrix} R_{ml}n_m n_l \delta_{ij} \\ -\frac{3}{2}R_{im}n_m n_j \\ -\frac{3}{2}R_{jm}n_m n_i \end{pmatrix} + C_{2w}\begin{pmatrix} \Pi_{ml2}n_m n_l \delta_{ij} \\ -\frac{3}{2}\Pi_{im2}n_m n_j \\ -\frac{3}{2}\Pi_{jm2}n_m n_i \end{pmatrix} \right] \frac{k^{3/2}}{C_l \varepsilon z}, \tag{21}$$

where n is the normal vector, $C_{1w} = 0.5, C_{2w} = 0.3$, and $C_l = 2.5$.

The turbulent kinetic energy (k) is

$$k = \frac{1}{2}(R_{11} + R_{22} + R_{33}), \tag{22}$$

where R_{11}, R_{22} and R_{33} are the normal stresses.

The transport equation for energy dissipation rate (ε) is

$$\frac{\partial}{\partial x_i}(\rho U_i \varepsilon) = C_\varepsilon \frac{\partial}{\partial x_i}\left[\frac{R_{ij}}{\varepsilon}k\frac{\partial \varepsilon}{\partial x_i} \right] + C_{1\varepsilon}\frac{1}{2}\frac{\varepsilon}{k}E_{ij}\cdot E_{ij} - C_{2\varepsilon}\frac{\varepsilon^2}{k}. \tag{23}$$

The six equations for Reynolds stress transport are solved along with a model equation for the scalar dissipation.

For heat transfer the model also provides solution of turbulence transport equations for each of the Reynolds heat fluxes.

2.3.2. The generalized gradient diffusion model (RSTM-1)

The algebraic stress model is used to obtain the turbulent heat fluxes, through the generalized gradient diffusion hypothesis for the scalar fluxes

$$R_{ih} = -C_h \frac{k}{\varepsilon} R_{im} \frac{\partial T}{\partial x_m},$$

where the coefficient $C_h = 0.3$.

2.3.3. Full flux transport equations for Reynold heat fluxes (RSTM-2)

Analogously to Eq. (15), the corresponding equation for the transport of the scalar flux R_{ih} considers the full flux transport equations of energy which takes the form

$$\frac{\partial}{\partial x_k}(U_k R_{ih}) = P_{ih} + \Lambda_{ih} - \varepsilon_{ih} + \Pi_{ih} + \Pi_{ih}^{\mathrm{w}}. \tag{24}$$

The production term (P_{ih}), diffusion (Λ_{ih}), dissipation (ε_{ij}), transport due to turbulent pressure (Π_{ih}) and the wall reflection (Π_{ih}^{w}) terms for the energy equations may be written as

Production term:

$$P_{ih} = -\left(R_{im} \frac{\partial T}{\partial x_m} + R_{mh} \frac{\partial U_i}{\partial x_m} \right). \tag{25}$$

Diffusion term:

$$\Lambda_{ih} = C_{h1} \frac{\partial}{\partial x_l} \left(\frac{k}{\varepsilon} R_{lm} \frac{\partial R_{ih}}{\partial x_m} \right) \tag{26}$$

with the constant diffusion coefficient C_{h1} taking the value of 0.15.

Dissipation rate: The viscous destruction term is neglected by invoking the local isotropic assumption of fine scale motion for high turbulent Reynolds numbers. Thus

$$\varepsilon_{ih} = (K_g + \mu) \overline{\frac{\partial u_i}{\partial x_k} \frac{\partial h}{\partial x_k}} = 0.$$

Pressure scrambling term:

$$\Pi_{ih} = \Pi_{ih1} + \Pi_{ih2} = -C_{1\theta} \frac{\varepsilon}{k} R_{ih} - C_{2\theta} P_{i\theta 2} \tag{27}$$

with $C_{1h} = 1.8$ and $C_{2h} = 0.6$.

The wall reflection term: The wall corrections to the pressure-scrambling terms are modelled by [20]

$$\Pi_{i\theta}^{w} = -C_{\theta w} \frac{k^{1/2}}{2.5 z_n} R_{kh} n_k n_i$$

where n is the normal vector and $C_{\theta w} = 0.5$.

The transport equations are solved for each individual component of the turbulent flux for every scalar.

2.4. Boundary conditions

Four boundary conditions are considered for each model, these are

Solid wall: Boundary conditions for velocity and heat flux, i.e.

$$U_i = 0$$

$\dot{q} =$ Constant over a specified area having 0.375 mm radius

$= 10^6$ W/m^2 (low heat flux case)

$= 10^7$ W/m^2 (high heat flux case)

Law of the wall conditions for standard k–ε model: The first computational point (P) close to the solid wall is considered in the turbulent sublayer. The velocity U_p at this point is assumed parallel to the solid boundary and has a logarithmic variation

$$|U_p| = \frac{U^*}{\kappa}\ln(\chi z_p^+); \quad k = \frac{U^{*2}}{\sqrt{C_\mu}} \quad \text{and} \quad \varepsilon = \frac{U^{*3}}{\kappa z} \tag{28}$$

where U^* and z_p^+, are the friction velocity and dimensionless distance from point P to the solid wall. These are defined as

$$U^* = \left(\frac{\tau_w}{\rho}\right)^{1/2}; \quad z_p^+ = \frac{\rho z_p U^*}{\mu} \tag{29}$$

where, τ_w is the shear stress at the wall, κ is the Von Karman constant, χ is a roughness parameter and z_p is the actual distance from the point P to the solid wall. For the turbulent layer z_p^+ is approximately between 10 and 400.

Boundary conditions for low-Reynolds number k–ε model: Laminar boundary conditions are set for the mean-flow variables, and the boundary conditions $k = 0$ and $d\varepsilon/dz = 0$ are introduced at the wall. The low-Reynolds number extension does not employ wall functions and the flow field needs to be meshed into the laminar sublayer and down to the wall. Consequently, the grid employed normal to the main flow direction is distributed so as to give a high concentration of grid cells near the wall. Therefore, the wall-adjacent node should be positioned at $z^+ = 1.0$ or even less.

Generalized wall functions for normal and shear turbulent stresses for the RSTM models: When the flow is very near the wall undergoes a rapid change in direction, the wall-functions approach is not successful in reproducing the details of the flow. Consequently the turbulent stresses and fluxes at the near wall grid points are calculated directly from their transport equations. In this case, the near-wall region lying between the wall and the near-wall computational node at z_p can be represented by two layers: the fully viscous sublayer, defined by $Re_v = z_v\sqrt{k_v}/\nu \cong 20$, and a fully turbulent layer. Based on the assumption that local equilibrium prevails in the turbulent layer, i.e. production equals dissipation for the turbulent kinetic energy, the above results

$$\frac{U_p}{\tau_w/\rho} C_\mu^{1/4}\sqrt{k_p} = \frac{1}{\kappa}\ln\left(\chi z_p \frac{C_\mu^{1/4}\sqrt{k_p}}{\nu}\right) \tag{30}$$

which yields the wall shear stress near the wall i.e.

$$\overline{vw}|_{z_v} = \tau_w/\rho,$$

this serves as the boundary condition for the $\overline{vw}$ transport equation.

In relation to normal stresses, the turbulence energy must decrease quadratically towards a value of zero [21] at the wall, therefore a zero-gradient condition for the normal stresses is physically realistic. This situation is insufficient to ensure an accurate numerical representation of near-wall effects. An improved approach for internal cells is needed in respect of evaluating volume-integrated production and dissipation of normal stresses (these are normally evaluated at cell centres, using linear interpolation, and then multiplied by the cell volume). Considering $\overline{v^2}$ as an example, the volume-integrated production of $\overline{v^2}$ between the wall and the P-node may be approximated by [22],

$$\int_{\Delta r}\int_{0}^{z_p} P_{22}\,\mathrm{d}\forall \cong \int_{\Delta r}\int_{z_v}^{z_p} -2\overline{vw}\frac{\partial V}{\partial z}\,\mathrm{d}\forall = 2\tau_w\left(\frac{V_p - V_v}{z_p - z_v}\right)z_p\Delta r, \tag{31}$$

where V_p and V_v follow from the log-law, equation (30). No contribution arises from the viscous sublayer since $\overline{vw} = 0$ in this layer. An analogous integration of the dissipation rate with the assumptions,

$$\varepsilon = \frac{2\nu k_v}{z_v^2}, \quad 0 \leqslant z \leqslant z_v,$$

$$\varepsilon = \frac{C_\mu^{3/4} k_p^{3/2}}{\kappa z_v}, \quad z_v \leqslant z < z_p,$$

leads to

$$\int_{\Delta r}\int_{0}^{z_p} \varepsilon\,\mathrm{d}\forall \cong \left[\frac{2\nu k_p}{z_v} + \frac{C_\mu^{3/4} k_p^{3/2}}{\kappa}\ln\left(\frac{z_p}{z_v}\right)\right]\Delta r, \tag{32}$$

an analogous treatment is applied to $\overline{v^2}$, while the production of $\overline{w^2}$ in the viscous and turbulent near wall layers region is zero.

The values resulting from Eqs. (31) and (32) are added, respectively, to the volume-integrated generation and dissipation computed for the upper half of the near-wall volume.

It should be noted that for the wall-law approach, the near-wall dissipation (ε_p) is not determined from its differential equation applied to the near-wall cell surrounding the node. Instead, and in accordance with the log law, this value is obtained via the length scale from

$$\varepsilon_p = \frac{C_\mu^{3/4} k_p^{3/2}}{\kappa z_p},$$

which serves as the boundary conditions for inner cells.

Inlet conditions: Temperature, velocity and boundary conditions need to be introduced

$$T = \text{constant (300 K)} \quad \text{and} \quad U_i = 300(1 - 2r^*)^{1/7}.$$

The values of k and ε are not known at the inlet, but can be determined from turbulent kinetic energy i.e.

$$k = \lambda\overline{u}^2, \tag{33}$$

where u is the average inlet velocity and λ is a percentage.

The dissipation is calculated from

$$\varepsilon = C_\mu\frac{k^{3/2}}{aD}, \tag{34}$$

where D is the diameter. The values $\lambda = 0.03$ and $a = 0.005$ are commonly used and may vary slightly in the literature [23].

Outlet: The flow is considered fully developed at the exit; in this case, flow boundaries extend over a long domain. Therefore, the condition for any variable ϕ is

$$\frac{\partial\phi}{\partial x} = 0, \tag{35}$$

where x is the arbitrary direction at the outlet.

Symmetry axis: At the symmetry axis, the radial derivative of the variables is set to zero, i.e.

$$\frac{\partial\phi}{\partial r} = 0, \tag{36}$$

Table 2
Property table

Property	Gas (Air)	
	Constant	Variable
Density ρ (kg/m^3)	1.189	p/RT
Thermal conductivity K (W/mK)	0.02565	$0.008103274 + 6.04893 \times 10^{-5}T$
Specific heat capacity c_p (J/kg K)	1005.0	$917 + 0.258T + 3.9804 \times 10^{-5}T^2$
Kinematic viscosity v (m^2/s)	1.544×10^{-5}	$-0.494679 \times 10^{-5} + 0.458394 \times 10^{-7}T + 0.80974 \times 10^{-10}T^2$

except

$$V = \overline{vw} = \overline{vh} = \overline{wh} = 0.$$

2.5. Variable properties

The equation of state is used for air, and the specific heat capacity and thermal conductivity are considered as a function of temperature for both air and steel. The properties employed are given in Table 2.

2.6. Local entropy generation

The non-equilibrium phenomenon existing in a flow system causes a continuous generation of entropy in the flow field. Every irreversible process can be viewed as the relevant flux driven by the associated potential. The flux of heat is driven by the temperature gradient and the flux of momentum is driven by the velocity gradient. The point-size control volume formulation of the second law gives [24]

$$S'''_{\text{gen}} = \rho \frac{\mathrm{D}s}{\mathrm{D}t} + \frac{\partial}{\partial x_i}\left(\frac{q_i}{T}\right) \geqslant 0$$

using the energy equation and the identity

$$\frac{\mathrm{D}e}{\mathrm{D}t} = T\frac{\mathrm{D}s}{\mathrm{D}t} + \frac{P}{\rho^2}\frac{\mathrm{D}\rho}{\mathrm{D}t},$$

the local entropy generation yields

$$S'''_{\text{gen}} = \frac{K_{\text{eff}}}{T^2}\left(\frac{\partial T_i}{\partial x_i}\right)^2 + \frac{\mu_{\text{eff}}}{T}\Phi \geqslant 0,$$

In two-dimensional polar coordinates

$$S'''_{\text{gen}} = \frac{K_{\text{eff}}}{T^2}\left[\left(\frac{\partial T}{\partial r}\right)^2 + \left(\frac{\partial T}{\partial z}\right)^2\right] + \frac{\mu_{\text{eff}}}{T}\left[2\left[\left(\frac{\partial V}{\partial r}\right)^2 + \left(\frac{V}{r}\right)^2 + \left(\frac{\partial W}{\partial z}\right)^2\right] + \left(\frac{\partial V}{\partial z} + \frac{\partial W}{\partial r}\right)^2\right]. \tag{37}$$

The first term on the right-hand side of Eq. (37) is the contribution due to finite heat transfer over finite temperature gradients, and the second term is the local volumetric entropy generation due to fluid friction. As it was stated in the previous study [16], Eq. (37) is valid for both laminar and turbulent flows; where, the effective thermal conductivity is the sum of the molecular thermal conductivity and the eddy thermal

conductivity, and the effective viscosity is the sum of the molecular viscosity and the eddy diffusivity. In turbulent flow, therefore, the local volumetric entropy generation depends upon the local spatial gradients of temperature, velocity, conductivity and viscosity. In this case, the conductivity and the viscosity may be written as

$$K = K_{\text{eff}} = K_{\text{l}} + K_{\text{t}}, \quad \mu = \mu_{\text{eff}} = \mu_{\text{l}} + \mu_{\text{t}}.$$

The local quantities of K_{eff} and μ_{eff} are computed for all the turbulence models used in the present study and the associated local volumetric entropy generation is determined.

A dimensionless temperature is introduced to assess the distribution in the flow field, i.e.

$$\theta = \frac{T_{\text{w}} - T_{\text{f}}}{T_{\text{w}} - T_{\text{jet}}}.$$

3. Numerical method and simulation

A control volume approach is employed when discretizing the governing equations. The discretization procedure is given in [25]. The problem of determining the pressure and satisfying continuity may be overcome by adjusting the pressure field so as to satisfy continuity. A staggered grid arrangement is used in which the velocities are stored at a location midway between the grid points, i.e. on the control volume faces. All other variables including pressure are calculated at the grid points. This arrangement gives a convenient way of handling the pressure linkages through the continuity equation and is known as semi-implicit method for pressure-linked equations (SIMPLE) algorithm. The details of this algorithm is given in [25].

The computer program developed enables to handle a non-uniform grid spacing. In each direction, fine grid spacing near the gas jet impinging point and the heated area is allocated while gradually increased spacing for locations away from the origin is considered. The grid generated in the present simulation is shown in Fig. 1. The grid independent tests are carried out by considering $76 \times 60, 152 \times 120$, 180×100 and 180×120. The number of grid points resulting grid independency are 180×120 in the y and z plane, respectively.

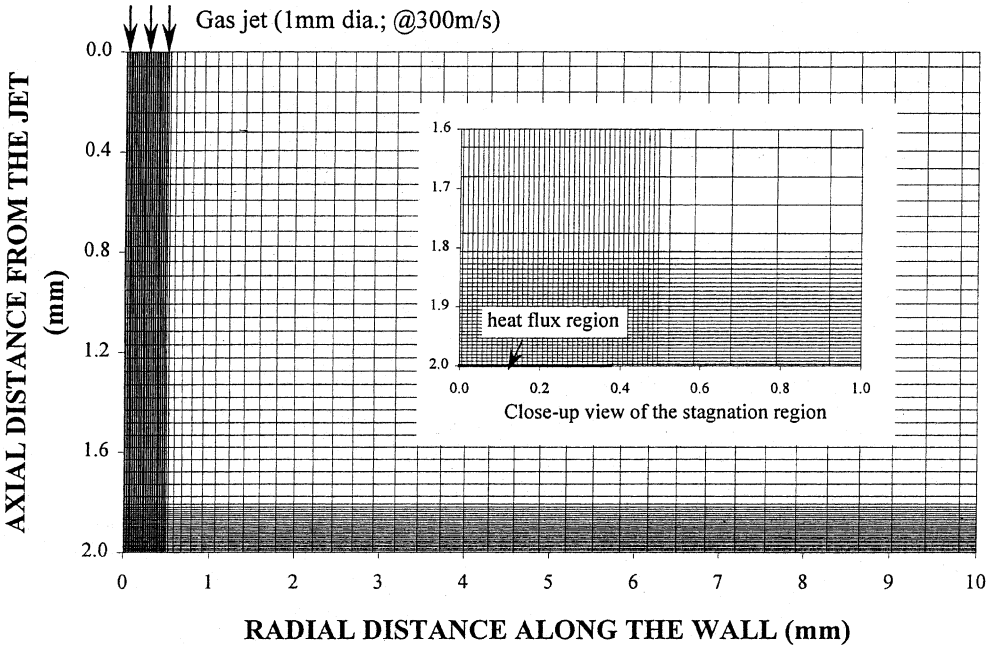

Fig. 1. Computational domain and the grid generated for numerical calculations.

4. Verification of the numerical predictions

In order to compare the present predictions with the previous experimental findings [11], jet Reynolds number and r/l are set as 23,000 and 2, respectively. The simulation conditions are given in Table 3.

The impinging turbulent axisymmetric jet flow is geometrically simple, it can be easily handled from a numerical point of view. It therefore, provides a convenient test case for turbulence model assessment.

Figs. 2 and 3 show the w'/W_{jet} (normalized root-mean-square turbulent velocity fluctuation), variation with dimensionless distance (z^*) for four turbulence models with constant and variable properties respectively, at $r^* = 1.0$. The k–ε turbulence model predicts higher values of w'/W_{jet} in the surface vicinity ($z^* \leqslant 0.05$) than the experimental findings [11] for both constant and variable properties. In this case, the near wall turbulent energy generation due to the turbulence models is more, which in turn results in relatively high levels of w'. This may be due to the use of the eddy-viscosity stress–strain law to present normal stress $\left(\overline{v'^2} = (2/3)k - 2\nu_t(\partial v/\partial z)\right)$, which results in a turbulence energy generation rate in the irrotational region close to the stagnation point of $3\nu_t(\partial v/\partial z)^2$. As the turbulence energy increases the turbulence viscosity (ν_t) increase, which in turn increases the k value. The RSTM model gives closer results to the experiment in the surface vicinity ($z^* \leqslant 0.05$). In the case of variable properties, as the dimensionless distance increases further, the k–ε and low-Reynolds number k–ε turbulence models result in almost the same trend of w'/W_{jet} provided that the RSTM model deviates considerably from w'/W_{jet} trend. In this case, Reynolds stress turbulence models result in low fluctuation velocities in the stagnation region because of the mixing of the jet before coming under the influence of the wall. When comparing constant and variable properties cases, the influence of density and viscosity are more pronounced on the RSTM models.

Table 3
Simulation conditions

Impinging fluid	Air
Jet Reynolds number	20000
Radius of heated area (mm)	0.375
r/l	2
Heat fluxes (W/m^2)	
Low	10^6
High	10^7

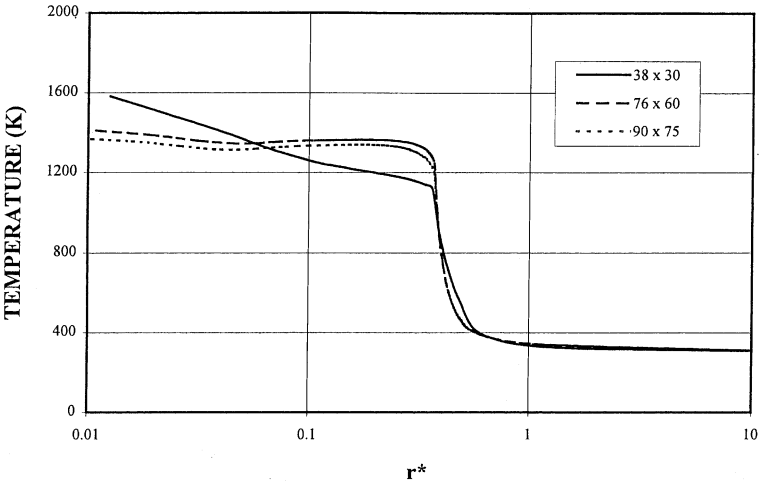

Fig. 2. Grid independence test obtained close to the wall for three grids using the k–ε low-Reynolds number model.

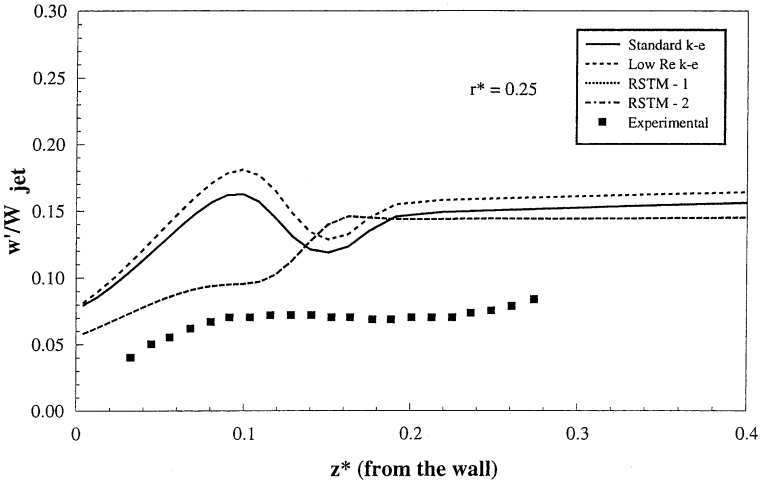

Fig. 3. Normalized axial velocity fluctuation versus z^* for four turbulence models and variable r^*. Experimental is from [11].

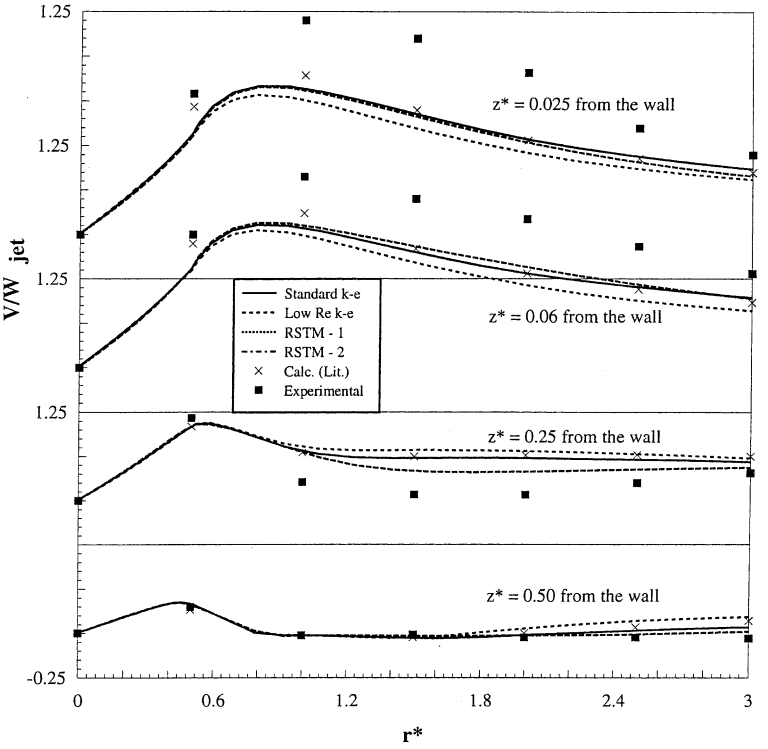

Fig. 4. Normalized radial velocity versus r^* for four turbulence models and variable z^*. Calc. (Lit.) indicates previous predictions [26]; Experimental is from [11].

Fig. 4 shows the comparison of numerically predicted and experimental profiles of normalized radial velocity for variable properties. The normalized radial velocity predicted from four turbulence models agrees well with the experimental findings at the jet axis, close to the solid surface. As the radial distance increases, the predictions close to the solid surface deviate from the experimental results. This starts when the normalized velocity reaches its maximum. It should be noted that the developing radial

flow in an axisymmetric geometry is moving into a continually enlarging area; in this case, the flow characteristics in axisymmetric flow differ slightly from those in a two-dimensional flow [26]. The prediction agrees well with the experimental findings as the axial distance from the solid surface increases. On the other hand, predictions of all the models approach close to the experimental findings at a region of $z^* \geqslant 0.25$.

5. Results and discussions

The results presented in this work cover the assessment of turbulence models based on the minimum entropy generation concept. In addition, the present predictions are validated by the previous experimental findings [11] and predictions [26].

Figs. 5 and 6 show the dimensionless temperature distribution in radial direction at different location along the jet axis for different turbulence models and heat fluxes. The dimensionless temperature close to the solid surface and across the jet differs for different turbulence models. This may be because of the low density and viscosity attainment close to the stagnation region. In this case, different turbulence models predict slightly different dimensionless temperatures in this region. Moreover, close to the

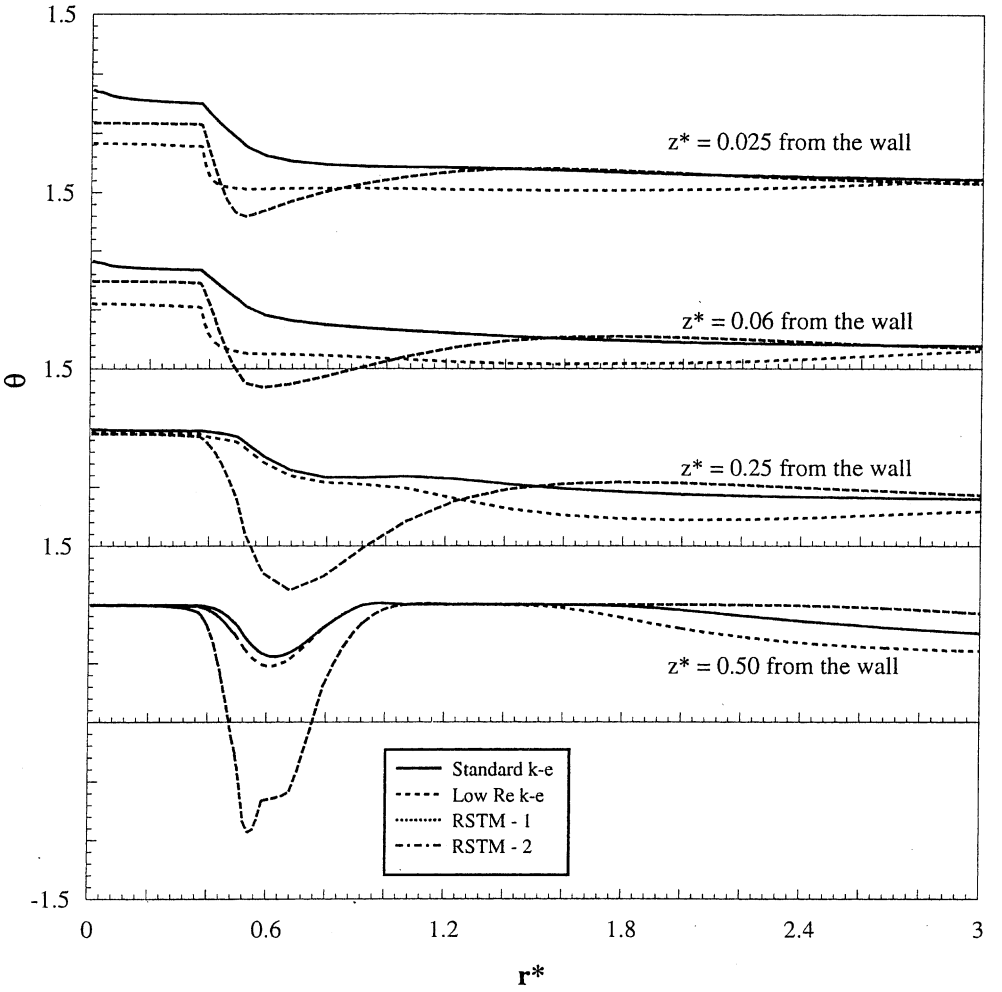

Fig. 5. Non-dimensional temperature distribution versus r^* at low heat flux for four turbulence models and variable z^*.

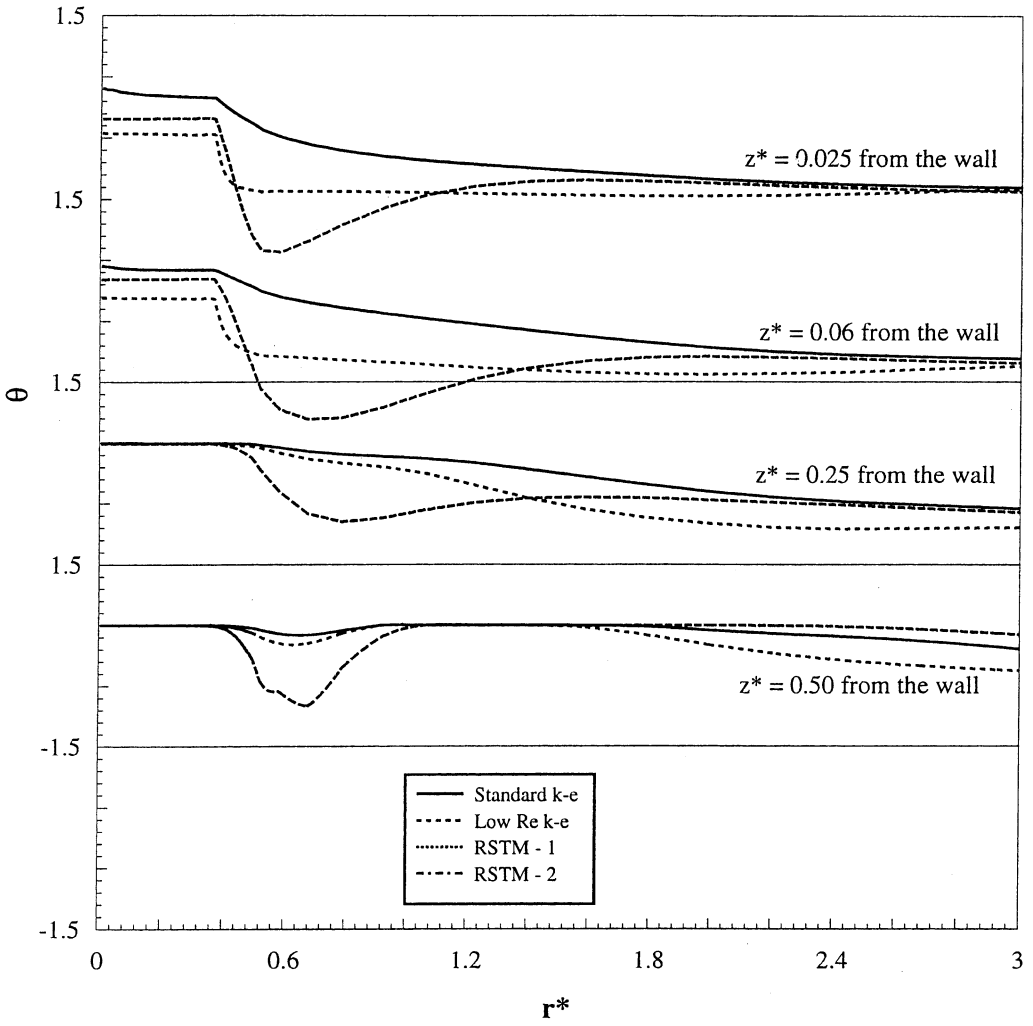

Fig. 6. Non-dimensional temperature distribution versus r^* at high heat flux for four turbulence models and variable z^*.

stagnation region, the turbulent mixing and radial velocity close to solid wall may not be substantiated resulting in less heat convection and high wall temperature. Consequently, the dimensionless temperature slightly increases in the stagnation region and as the distance from the surface increases, dimensionless temperature in the radial direction becomes more uniform. As the distance from the solid wall increases towards the gas jet, the dimensionless temperatures resulting from all turbulence models attain close values across the heated area. On the other hand, small drop in dimensionless temperature occurs in the vicinity of the heated spot. This may be attributed to the low wall temperature and mixing of the impinging jet with the heated fluid close to the heated surface. The RSTM model, however, results in relatively lower dimensionless temperature in this region as compared to other turbulence models. As the distance from the surface and the radial direction increases, the dimensionless temperature associated with all turbulence models attains almost the same value. It is therefore, expected that all the turbulence models give similar temperature distribution as the distance from the surface and radial distance increase.

Figs. 7 and 8 show the logarithimic values of constant volumetric entropy generation lines ($\log_{10}(S'''_{\text{gen}})$) due to heat transfer and fluid friction at two constant heat fluxes for four turbulence models. The constant S'''_{gen} lines due to fluid friction are similar in the far field for all turbulence models, except standard k–ε model. This deviation is more pronounced at high heat flux (Fig. 8); in this case, the volumetric entropy

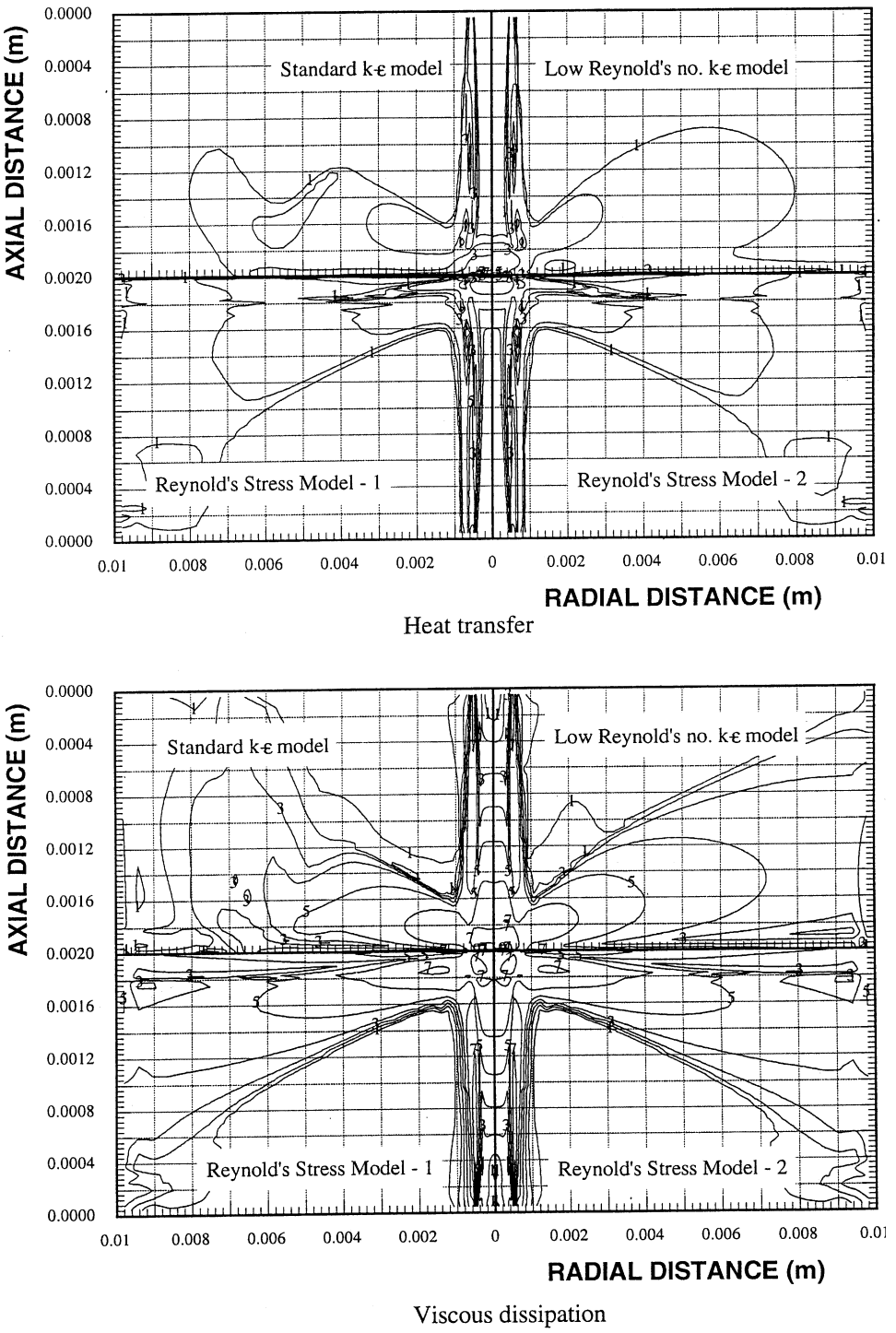

Fig. 7. Entropy contours obtained from four different turbulence models due to heat transfer and viscous dissipation for low heat flux.

generation is higher in region away from the stagnation. The constant S'''_{gen} lines due to fluid friction are identical for RSTM-1 and RSTM-2 turbulence models. In general, constant S'''_{gen} lines attain high values close to the stagnation region, and across the shear layer between the gas jet and the surrounding fluid. The volumetric entropy generation due to fluid friction is higher than that corresponds to heat transfer. This

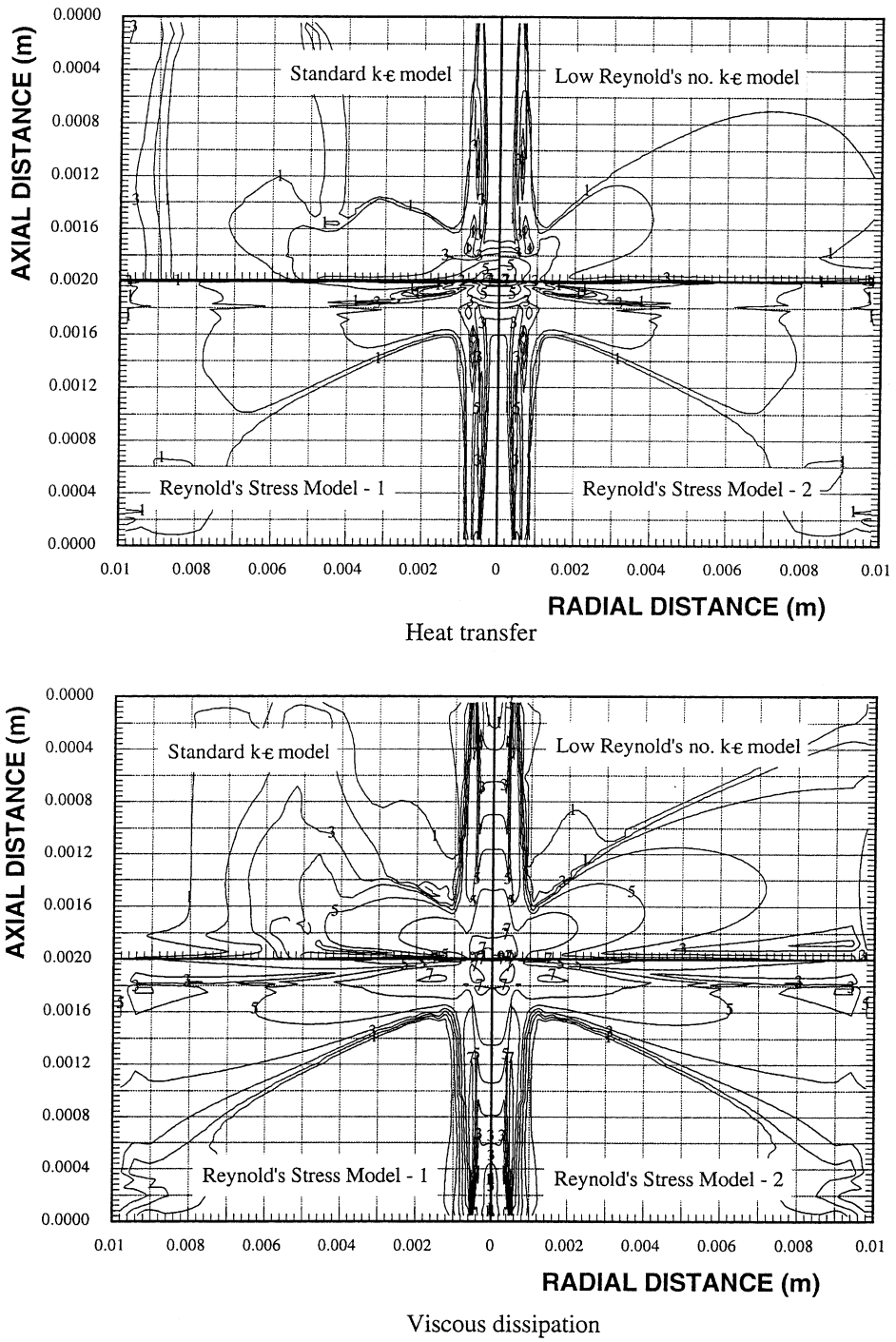

Fig. 8. Entropy contours obtained from four different turbulence models due to heat transfer and viscous dissipation for high heat flux.

may be due to the amount of heat supplied from solid surface to the fluid which may not be substantial to generate large temperature gradient in the surface vicinity. In this case, the temperature gradients become less, which in turn results in low volumetric entropy generation rate. The heat flux has significant effect on the entropy production rate in the far field, but it has almost no-effect on the S'''_{gen} distribution over the region of stagnation.

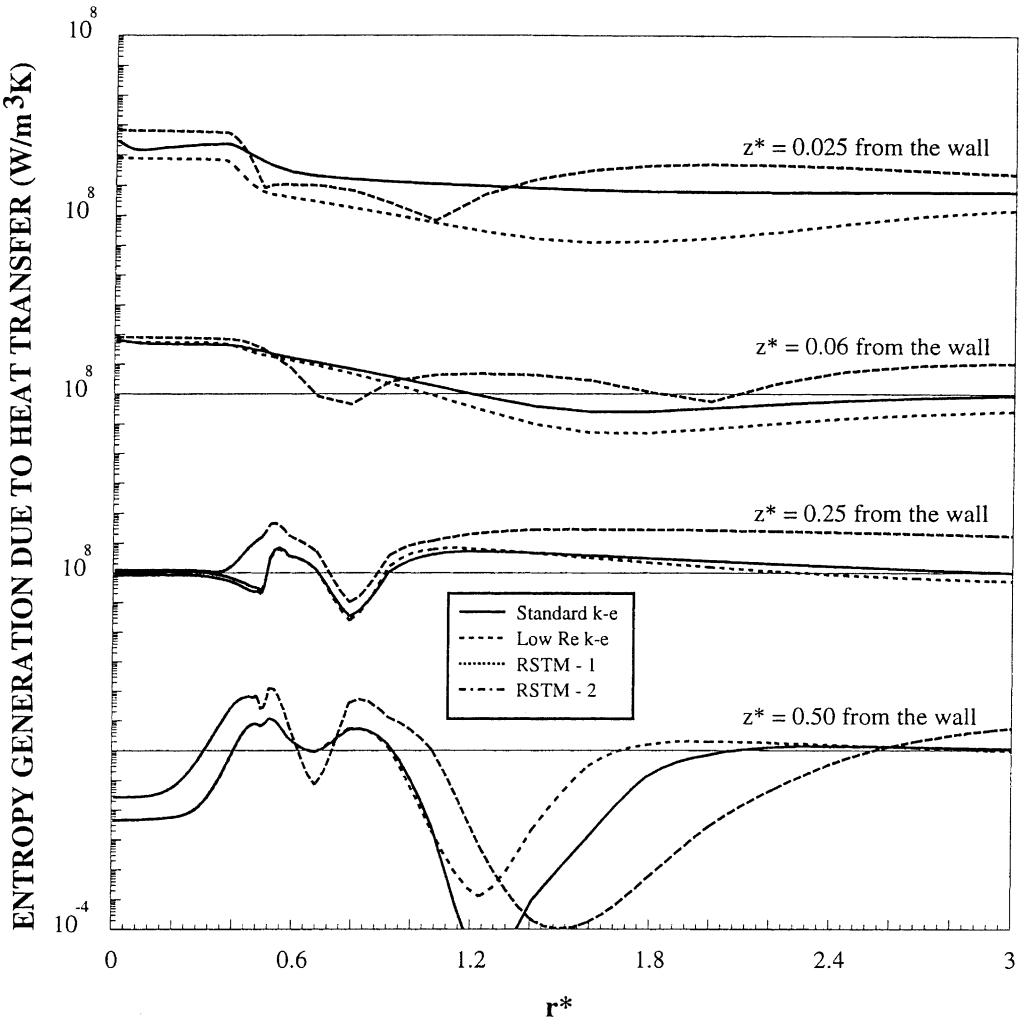

Fig. 9. Volumetric entropy generation due to heat transfer at low heat flux for four turbulence models and variable z^*.

Figs. 9 and 10 show, the volumetric entropy generation due to heat transfer in the radial distance at different jet axis locations for four turbulence models and two heat fluxes. The volumetric entropy generation reaches the highest value close to the heated region for a high heat flux case. This may be due to the temperature gradient attainment in this region. The RSTM-1 and low-Reynolds number k–ε model predict the lowest volumetric entropy generation across the heated spot at $z^* = 0.025$. As the distance from the surface increases volumetric entropy generation predicted from all turbulence models attain almost the same values across the heated spot. Moreover, the entropy generation in the region slightly beyond the heated spot fluctuates for $z^* \geqslant 0.06$. The radial distance where the fluctuation occurs becomes close to the heated spot centre as the distance from the surface increases. This may occur because of the mixing of the impinging gas jet with the heated fluid in this region. On the other hand, low-Reynolds number k–ε model results in high volumetric entropy generation as the axial distance from the solid surface to nozzle increases for the high heat flux case. This may be due to the fact that low-Reynolds number model predicts slightly high temperature gradients in the flow field, which may also be observed from Fig. 6. When comparing Figs. 9 and 10, it may be seen that the influence of heat flux on the volumetric entropy generation is not substantial in the stagnation region, the visible effect occurs only at $z^* \leqslant 0.06$ above the solid surface and across the heated region. In this case, at low heat flux all turbulence models give almost the same volumetric entropy values, but this case differs slightly at high heat flux.

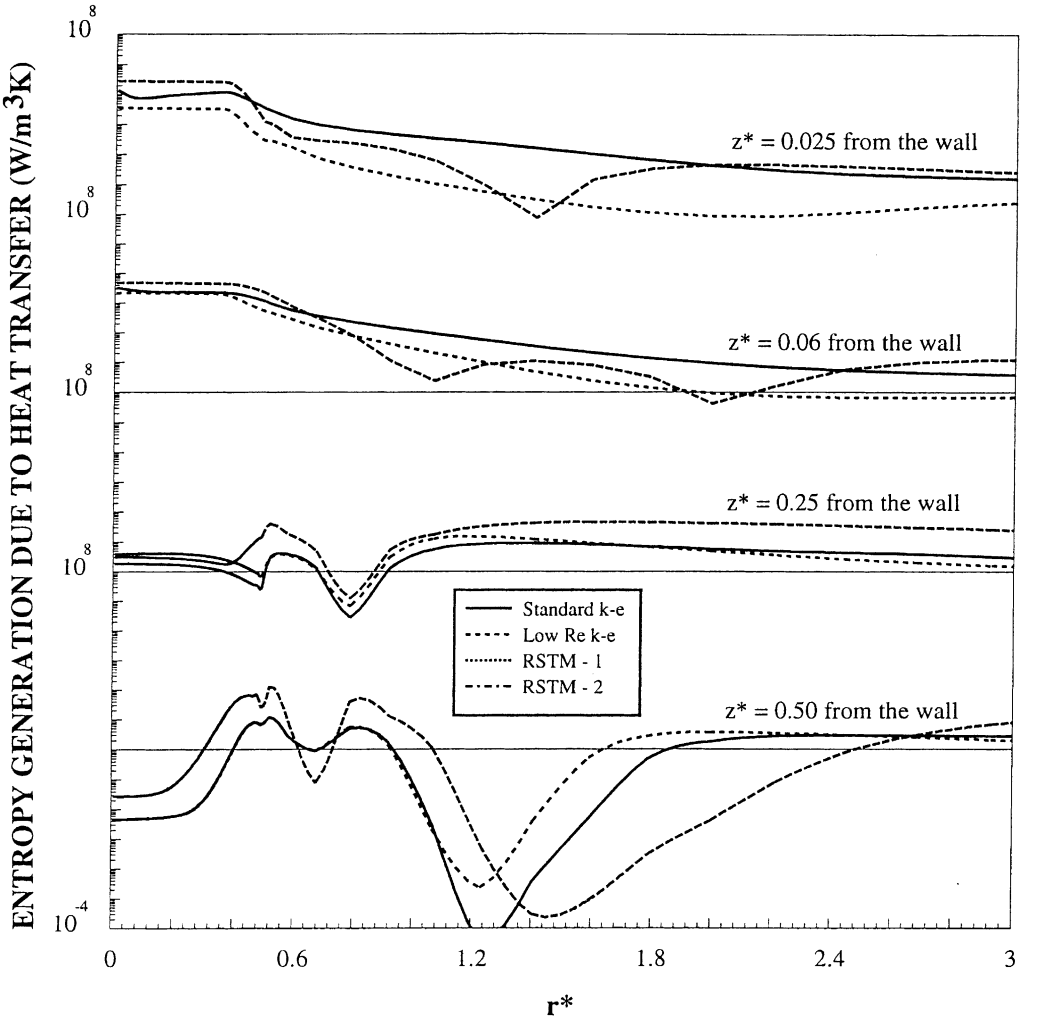

Fig. 10. Volumetric entropy generation due to heat transfer at high heat flux for four turbulence models and variable z^*.

Fig. 11 shows the frictional volumetric entropy generation in the radial direction for four turbulence models as the axial distance is variable. The volumetric entropy generation increases in the stagnation region across to the jet. This is because of the considerable kinetic energy loss in this region. The maximum volumetric entropy generation is produced in the stagnation region $z^* \leqslant 0.06$. RSTM-1 and RSTM-2 models predict higher volumetric entropy generation in the stagnation region than k–ε turbulence models. This may be due to the considerable density and viscosity variation in this region, i.e. because of heat transfer the density and viscosity vary considerably. As the radial distance increases in the region close to the solid wall, the volumetric entropy generation predicted from RSTM-1 and RSTM-2 models increases further. The effect of shear layer, between the jet and its surrounding, on the volumetric entropy generation becomes visible as z^* increase to 0.5 above the solid surface. On the other hand, the volumetric entropy generation reduces considerably in the far field of the flow ($1.8 < r^* < 3$ and $z^* \leqslant 0.25$).

Table 4 gives the total entropy generation due to fluid friction and heat transfer in the field ($0 \leqslant z^* \leqslant 0.25$ and $0 \leqslant r^* \leqslant 1.0$) for two heat fluxes. The low-Reynolds number k–ε model results in minimum entropy generation in this region. RSTM and standard k–ε model predict slightly high entropy generation. The influence of heat flux on the entropy generation is not significant, since the entropy generation due to two heat fluxes are almost similar. It should be noted that the heat fluxes introduced in the present study are small

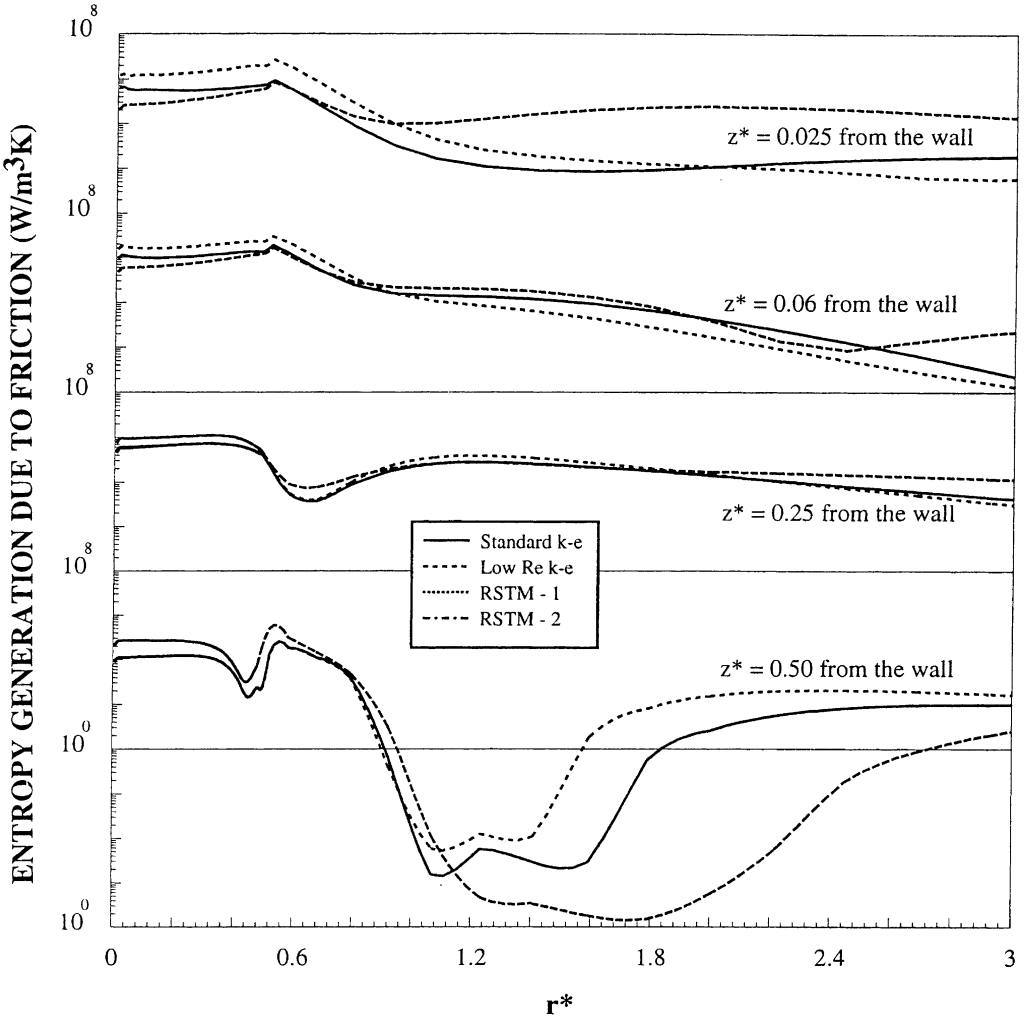

Fig. 11. Volumetric entropy generation due to friction for four turbulence models and variable z^*.

Table 4
Volumetric entropy generation in the near field for two heat fluxes

	Turbulence models	Volumetric entropy generation due to fluid friction (W/m^3 K)	Volumetric entropy generation due to heat transfer (W/m^3 K)
Low heat flux	k–ε model	5.09E−05	1.4E−06
	Low-Reynolds number k–ε model	1.51E−05	2.473E−06
	RSTM-1 model	5.88E−05	2.51E−06
	RSTM-2 model	6.59E−05	7.41E−07
High heat flux	k–ε model	3.54E−05	1.202E−05
	Low-Reynolds number k–ε model	7.05E−06	1.46E−05
	RSTM-1 model	3.20E−05	1.48E−05
	RSTM-2 model	3.74E−05	7.94E−06

enough not to generate considerably high temperature gradient in the flow field. The low-Reynolds number and k–ε models result in lower total entropy generation in the whole field as compared to RSTM models. Thus the influence of heat flux on the entropy generation becomes very minor in the far field.

6. Conclusions

The numerical scheme introduced in the present study successfully predicts the flow field and local volumetric entropy generation for four turbulence models with reasonable accuracy. When comparing the present predictions and previous experimental findings, the Reynolds stress turbulent models predict the flow field in the region where $z^* \leqslant 0.05$ more realistically as compared to other turbulent models employed. However, as z^* increases $(0.05 \leqslant z^* \leqslant 0.3)$ the k–ε and low-Reynolds number k–ε models predict similar w'/W_{jet} to that obtained from the experiment. The entropy analysis enables to identify the viscous dissipation in the flow field. Moreover, the minimum entropy generation concept alone cannot be used to evaluate the various turbulence models but the entropy analysis results should be accompanied with the experimental findings when assessing the turbulence models. In the present study, S'''_{gen} predicted in the stagnation region, where main contribution of the entropy generation occurs in this region, is less for low-Reynolds number k–ε model than RSTM models. The specific conclusions derived from the present study however, may be listed as follows:

1. The flow field developed due to various turbulence models agrees well with the experimental findings in the region above the solid wall. Radial velocity profiles corresponding to various turbulence models show that the Reynolds stress model prediction agrees better with the experimental finding than that corresponding to k–ε and low-Reynolds number k–ε models in the stagnation region $(z^* \leqslant 0.05)$.
2. The dimensionless temperature attains the highest and the lowest values for RSTM-1 and low-Reynolds number k–ε models respectively, in the stagnation region $(0.05 \leqslant z^* \leqslant 0.3)$. As the radial distance increases, the dimensionless temperature associated with all turbulent models attains almost the same value, i.e. the temperature distribution predicted due to turbulence models becomes almost the same in the far field.
3. The local volumetric entropy generation attains higher values close to the stagnation region and across the shear layer between the jet and the surrounding fluid. The volumetric entropy generation due to heat transfer is slightly lower than that due to fluid friction. The constant S'''_{gen} lines due to fluid friction are similar in the far field for all turbulent models, except for standard k–ε model, and this deviation is more pronounced at high heat flux. The heat flux has considerable effect on S'''_{gen}, but this effect is minimal for $z^* \geqslant 0.25$.
4. Low-Reynolds number k–ε model predicts the minimum volumetric entropy generation close to the stagnation region. Moreover, the RSTM models predict slightly high volumetric entropy generation as the radial distance from the stagnation region extends. This increase, however, is not substantiated.

References

[1] J.N.B. Livingood, P. Hrycole, Impingement heat transfer from turbulent air stream jets to flat plates – a literature survey, Technical Report TM X-2778, NASA, 1973.
[2] J.F. Brison, G. Brun, Round normally impinging turbulent jets, in: Proceedings of the 15th International Association for Hydraulic Research, Working Group on Refined Flow Modelling, Lyon, 1991.
[3] K. Jambunathan, E. Lai, M.A. Moss, B.L. Button, A review of heat transfer data for single circular jet impingement, Int. J. Heat Fluid Flow 13 (1992) 106–115.
[4] M.M. Gibson, R.D. Harper, Calculation of impinging jet heat transfer with the low-Reynolds number q–ζ turbulence model, Int. J. Heat Fluid Flow 18 (1997) 80–87.
[5] D.H. Lee, Y.S. Chen, S.D. Kim, Turbulent flow and heat transfer measurements on a curved surface with a fully developed round impinging jet, Int. J. Heat Fluid Flow 18 (1997) 160–169.
[6] K. Nishino, M. Samada, K. Kesua, K. Torii, Turbulence statistics in the stagnation region of an axisymmetric impinging jet flow, Int. J. Heat Fluid Flow 17 (1996) 193–201.
[7] W. Rodi, N.N. Mansour, V. Michelossi, One-equation near-wall turbulence modeling with the aid of direct simulation data, J. Fluids Engrg. 115 (1993) 196–201.
[8] G.K. Morris, S.V. Gaimella, R.S. Amano, Prediction of jet impingement heat transfer using a hybrid wall treatment with different turbulent Prandtl number functions, J. Heat Transfer 18 (1996) 562–569.
[9] R.S. Amano, H. Brandt, Numerical study of turbulent axisymmetric jets impinging on a flat plate and flowing into an axisymmetric cavity, J. Fluids Engrg. 106 (1984) 410–417.
[10] B.M. Tchavdarov, Two-dimensional vortex dynamics of inviscid–viscous interaction at turbulent gas jet impingement, Int. J. Heat Fluid Flow 18 (1997) 316–327.

[11] D. Cooper, D.C. Jackson, B.E. Launder, G.X. Liao, Impinging jet studies for turbulence model assessment – I. Flow-field experiments, Int. J. Heat Mass Transfer 36 (36) (1993) 2675–2684.
[12] A. Bejan, Thermodynamics of an isothermal flow: the two-dimensional turbulent jet, Int. J. Heat Mass Transfer 34 (2) (1991) 407–413.
[13] A. Bejan, Entropy generation minimization: the new thermodynamics of finite-size devices and finite-time processes, J. Appl. Phys. 79 (3) (1996) 1191–1218.
[14] V.S. Arpaci, A. Selamet, Entropy efficiency of energy systems, Prog. Energy Combust. Sci. 18 (1992) 429–445.
[15] A. Bejan, The thermodynamic design of heat and mass transfer processes and devices, Int. J. Heat Fluid Flow 8 (4) (1987) 258–276.
[16] M.K. Drost, M.O. White, Numerical predictions of local entropy generation in an impinging jet, J. Heat Transfer 113 (1991) 823–829.
[17] S.Z. Shuja, B.S. Yilbas, M.O. Budair, Stagnation point flow over constant heat flux surface: various turbulence models, Proceed. CSME FORUM 98, 1 (1998) 210–217.
[18] T.B. Gatski, M.Y. Hussaini, J.L. Lumley, Simulation and Modeling of Turbulent flows, Oxford University Press, New York, 1996.
[19] B.E. Launder, W. Rodi, The turbulent wall jet – measurement and modeling, Ann. Rev. Fluid Mech. 15 (1983) 429–433.
[20] T.J. Craft, Second-moment modeling of turbulent scalar transport, Ph.D. Thesis, Faculty of Technology, University of Manchester, 1991.
[21] C. Benocci, Introduction to the modeling of turbulence 1991-02, Von Karman Institute for Fluid Dynamics, March 1991.
[22] S. Hogg, M.A. Leschziner, Second-moment-closure calculation of strongly swirling confined flow with large density gradients, Int. J. Heat Fluid Flow 10 (1) (1989) 16–27.
[23] P. Bradshaw, T. Cebeci, J.H. Whitelaw, Engineering Calculation Methods for Turbulent Flow, Academic press, New York, 1981 (chapter 3, p. 51).
[24] A. Bejan, Entropy Generation Minimization, first ed., CRC Press, New York, 1995.
[25] S.V. Patankar, Numerical Heat Transfer, McGraw-Hill, New York, 1980.
[26] S. Ashforth-Frost, K. Jambunathan, Numerical prediction of semi-confined jet impingement and comparisons with experimental data, Int. J. Numer. Methods Fluids 23 (1996) 295–306.